Nano Research

Open Access

Research Article

Atomic-scale origins of ultraviolet-driven phase transition behavior in strongly correlated vanadium dioxide heterostructures

Tao Zhao[1], Hongyi Ouyang[1], Jinxin Gu[2], Yanyu Chen[1], Xingquan Guo[1], Qianqian Zhao[1], Jiarui Lu[1], Chao Li[1], Yanfei Yang[1], Haobo Fan[1], Shuliang Dou[1] ✉, Jiupeng Zhao[3] ✉, and Yao Li[1] ✉

[1] *Center for Composite Materials and Structure, Harbin Institute of Technology, Harbin 150001, China*
[2] *Suzhou Laboratory, Suzhou 215123, China*
[3] *School of Chemistry and Chemical Engineering, Harbin Institute of Technology, Harbin 150001, China*

Cite this article: *Nano Research*, **2026**, *19*, 94908919. https://doi.org/10.26599/NR.2026.94908919

ABSTRACT: Precise control over multiple functional phases in strongly correlated VO_2 and its heterostructures establishes a correlation between inclusions, defect dynamics and the stabilization of monoclinic versus tetragonal phases. However, a comprehensive atomic-level understanding of these processes remains insufficient to elucidate the underlying multiple defect-phase relationship mechanisms. Herein, we uncover the atomic-scale interlayer defect transfer mechanism in VO_2-based Fabry−Pérot resonant cavity heterostructures under vacuum-ultraviolet (VUV) irradiation. The irradiation induces cleavage of In–O and Sn–O bonds within the indium-tin-oxide (ITO) layer, triggering the concerted diffusive migration of In, Sn, and oxygen vacancies with VO_2. This migration elevates electron occupancy in the hybridized energy levels of the $d_{//}$-bond orbital and In/Sn-d orbitals within V–V dimers. The enhanced $d_{//}$ electron density strengthens orbital overlap with π* antibonding orbitals, driving the VO_2 phase transition from insulating monoclinic to metallic rutile. These results offer important theoretical and experimental insights into defect-mediated phase engineering in strongly correlated oxides and hold promise for advancing applications in quantum optoelectronic information and adaptive optics.

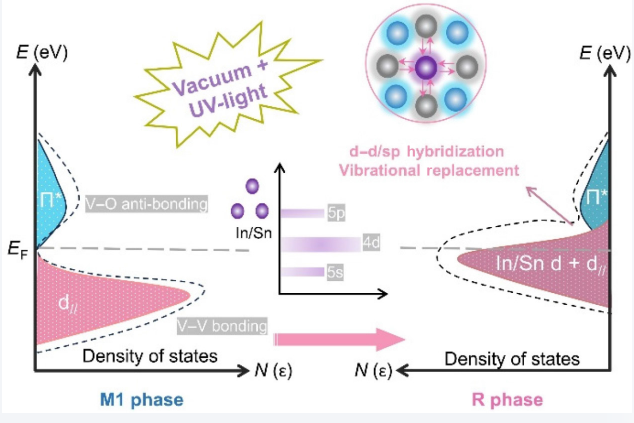

KEYWORDS: VO_2 phase transition, strongly correlated oxide, defect migration, vacuum ultraviolet, heterostructure

1 Introduction

The precise control of multiple functionalities in strongly correlated oxide vanadium dioxide (VO_2) and its heterostructures remains a central challenge, owing to their extreme sensitivity to external stimuli. By navigating neighboring minima in the free energy landscape—governed by parameters such as temperature, magnetic field, doping, and high-energy light irradiation—it becomes possible to induce atomic rearrangements, driving phase transitions between the insulating and metallic phases [1–3]. A defining feature of correlated electron systems is the profound influence of intrinsic and extrinsic atomic defects on d-band filling under various stimuli [4]. Strong electronic correlations, coupled with structural transitions, lead to dramatic modifications in the electronic structure, manifesting in emergent electronic, ferroelectric, optical, and magnetic properties [5]. These tunable functional properties have enabled diverse applications, including neuromorphic computing [6], thermochromic smart windows [7], memristors [8], dynamic thermal management systems [9], and deformation-toughened materials [10].

As a prototypical strongly correlated oxide, VO_2 exhibits defect-dependent phase stability that is critical for property engineering. Intrinsic defects, particularly oxygen vacancies, dramatically influence electronic performance through redox-mediated conductivity modulation, where vacancy concentrations directly govern charge transport characteristics [11]. Extrinsic doping provides an additional degree of control, enabling tailored insulator-to-metal transitions that can be either reversible or irreversible at

Received: February 27, 2026; **Revised:** June 7, 2026
Accepted: June 8, 2026

✉Address correspondence to Yao Li, YaoLi@hit.edu.cn; Jiupeng Zhao, jpzhao@hit.edu.cn; Shuliang Dou, dousl@hit.edu.cn

temperatures below the characteristic 68 °C transition threshold [12]. For example, tungsten substitution in the vanadium sublattice demonstrates particularly pronounced effects: its large ionic radius induces substantial anisotropic strain while its hexavalent state drives electron doping, collectively destabilizing the low-temperature M1 phase relative to the metallic state [13]. Alternative dopants produce distinct structural consequences—Cr and Al preferentially stabilize the M2 phase through either substitutional doping or epitaxial strain [14, 15], interstitial hydrogen induces orthorhombic phase formation while enabling room-temperature stabilization of the metallic rutile phase [16], and boron interstitials selectively promote the R phase over M1 [17]. Although these empirical observations establish a clear correlation between inclusion-related defect dynamics and phase stabilization (monoclinic versus tetragonal phases), a comprehensive atomic-level understanding of these processes that elucidates the underlying multiple defect-phase relationship mechanisms remains insufficient.

Herein, we elucidate the mechanism by which the evolution of interlayer oxide defects affects the phase transition of VO_2 in Fabry–Perot resonant cavity (V-FPRC) structure under vacuum UV irradiation. This mechanism at the atomic scale is clearly evidenced by a combination of techniques, including high-angle annular dark-field scanning transmission electron microscopy (HAADF-STEM), X-ray absorption near-edge structure (XANES), extended X-ray absorption fine structure (EXAFS), selected area electron diffraction (SAED), deep-etching X-ray photoelectron spectroscopy, and photo-induced force microscopy (PiFM). The phase transition from monoclinic (M) to rutile (R) in VO_2 is attributed to the interlayer diffusion of indium (In), tin (Sn), and V_O within the V-FPRC structure. The hybridization-induced energy level alignment between the d-orbitals of In/Sn and the bonding $d_{//}$ orbitals of V–V dimers leads to vibrational replacement. Consequently, this process induces a distinct shift from the $d_{//}$ bonding orbital to the π^* antibonding orbital in VO_2. These findings offer substantial theoretical and experimental insights that advance the rational design of defect-engineered strongly correlated oxides for quantum optoelectronic information science applications.

2 Results and discussion

2.1 Observation of V-FPRC macroscopic infrared (IR) optical response under UV-irradiation

In this study, the V-FPRC sample before vacuum-UV irradiation was designated as the pristine sample, while the sample after irradiation was termed the irradiated sample. To efficiently assess the optical response behaviour of the VO_2 phase structure, the layered structure of the V-FPRC is illustrated in Fig. 1(a), where the Fabry–Pérot (F–P) cavity, with a layered structure of Al/HfO_2/VO_2/indium-tin-oxide (ITO) (high-resistance and infrared-transmittance), functions as a thermally infrared regulator [18]. This design facilitates tunable infrared emission (2.5–25 μm), enabling dynamic control of radiative heat transfer. Below the phase transition temperature (T_c), VO_2 exists in an insulating state, wherein the resonant cavity is absent. In this regime, incident IR light transmits through the ITO/VO_2/HfO_2 multilayer stack and undergoes high reflection (low emissivity) at the Al interface. Upon exceeding the phase transition temperature, VO_2 undergoes a reversible transition to a metallic state, forming a F–P resonant cavity composed of ITO/VO_2/HfO_2/Al. This structural configuration facilitates multiple reflections and constructive interference of IR light within the cavity, resulting in strong absorption (high emissivity). Correspondingly, PiFM provides nanoscale optical imaging capabilities surpassing the diffraction limit (Fig. 1(a)). This technique employs wavelength-tuned infrared laser illumination of an atomic force microscope's (AFM) metallized tip, generating a strongly confined evanescent field at the tip apex. Analysis of the resulting near-field interactions enables direct mapping of local compositional variations at the nanoscale [19].

The cross-sectional transmission electron microscopy (TEM) and energy-dispersive X-ray spectroscopy (EDX) mapping images of the V-FPRC reveal that the thicknesses of the Al, HfO_2, VO_2, and ITO layers are 150, 600, 50, and 30 nm, respectively (Fig. S1 in the Electronic Supplementary Material (ESM)). To assess the regulation of thermal infrared optics of the V-FPRC samples before and after irradiation, the Fourier transform infrared reflectance spectra (FTIR) were obtained. As in Fig. 1(b), the pristine V-FPRC in its two states exhibits notable variations across the 2.5–25 μm range, by contrast, the irradiated V-FPRC infrared radiation modulation capability disappears. Subsequently, the emissivity of irradiated V-FPRC increases from 0.29 to 0.53 at 0 °C, and the IR-emissivity regulation ($\Delta\varepsilon$) decreases from 0.34 to 0.01 (Fig. 1(c)). Nano-IR amplitude PiFM data were acquired at a detection frequency of $\omega \approx$ 820 and 1000 cm^{-1} (10 μm), corresponding to the photophonon (OPhs) modes of the M1-phase VO_2 and F–P modes [20, 21]. As shown in Figs. 1(d) and 1(e), the PiFM signal imaging of the irradiated sample revealed no significant changes between the insulating (I) and metallic (M) states, along with the disappearance of the M1-phase V–V dimer phonon vibration. These observations further support the optical nature of the degradation in dynamic IR-regulation.

To further investigate the degradation of IR modulation performance in V-FPRC after vacuum UV irradiation, a series of material phase characterizations were conducted. The grazing-incidence X-ray diffraction (GIXRD) patterns of irradiated V-FPRC reveal VO_2's R-phase (27.6°, (110)), in contrast to the M1-phase (27.8°, (110)) dominant in the pristine sample (Figs. S2(a) and S2(b) in the ESM) [22, 23]. Using the HfO_2(200) peak area in each V-FPRC sample as a benchmark, we observed a 3.5-fold increase in the ITO(222) peak area for irradiated V-FPRC (Fig. S2(c) in the ESM), alongside a 2.4-fold enhancement in the VO_2 R-phase (110) peak area (Fig. S2(e) in the ESM), while the HfO_2(011) peak area remained unchanged (Fig. S2(d) in the ESM) [24, 25]. This is further confirmed by SAED and cross-sectional TEM images, where the HfO_2 layer for irradiated V-FPRC shows distinct diffraction spots at the ($\bar{1}$11) crystal planes, confirming results consistent with the pristine V-FPRC crystallinity (Fig. S3 in the ESM). These results indicate that UV irradiation enhances the crystallinity of both the ITO and VO_2 layers in V-FPRC. In contrast, the loss of IR modulation capability in V-FPRC is primarily attributed to phase alterations in the ITO and VO_2 layers.

2.2 UV-irradiation effect on ITO/VO_2 heterojunction interface of V-FPRC

Cross-sectional STEM was performed to gain deeper insight into the ITO/VO_2 morphology and crystal structure of the pristine and irradiated V-FPRC. Figures 2(a) and 2(b) depict STEM images of a cross section of the V-FPRC, the representative selected area in the cross section consists of the ITO on top of the VO_2 layer also including the interface, and the blue and red regions correspond to

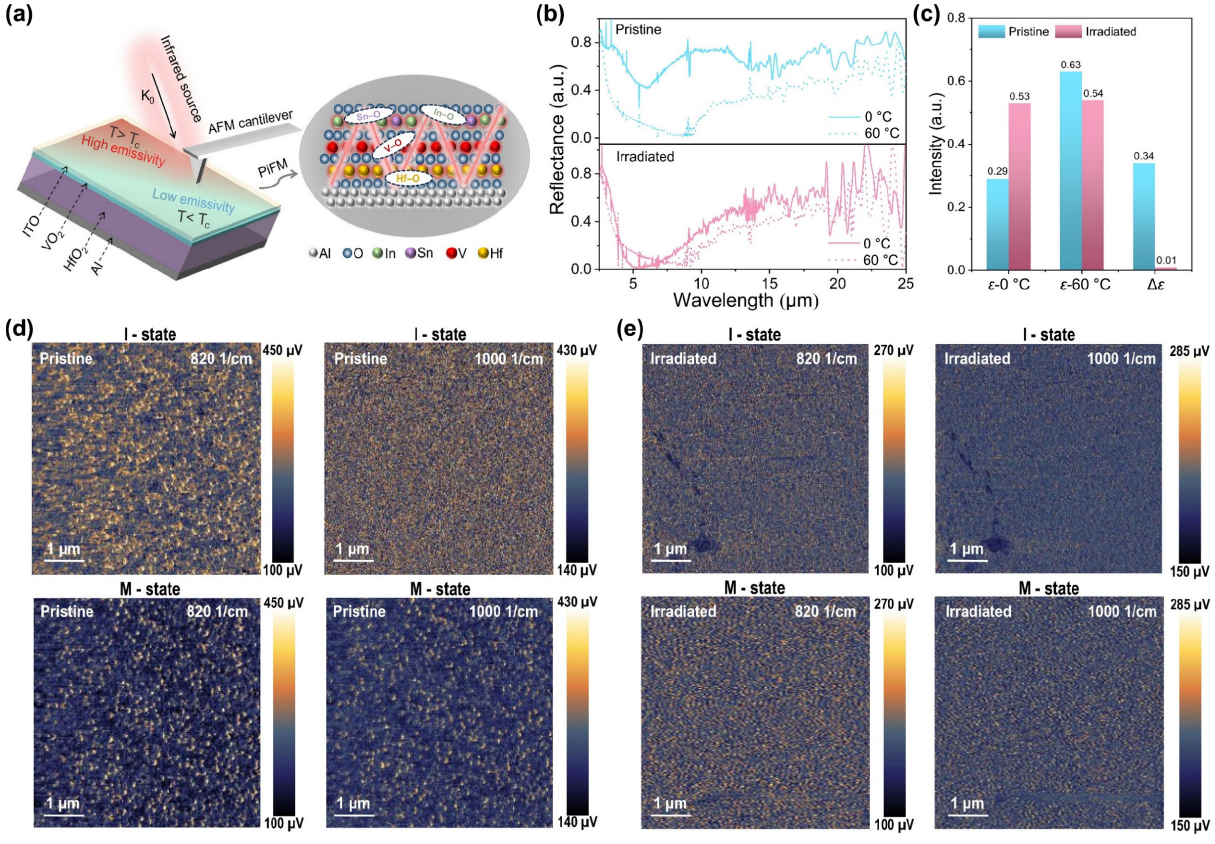

Figure 1 Infrared optics testing of V-FPRC thermal radiation before and after irradiation. (a) Schematic of the experiment PiFM and the structure of the V-FPRC. (b) Infrared reflectance spectra of the pristine and irradiated V-FPRC at 0 and 60 °C. (c) Emittance values of pristine and irradiated V-FPRC. (d) and (e) Experimental PiF signal imaging mapping of the near-field amplitude of the pristine and irradiated V-FPRC, PiFM data collected in the I-state (20 °C) and M-state (60 °C) at the frequency $\omega \cong 820\ cm^{-1}$ and $\omega \cong 1000\ cm^{-1}$ (10 μm), representing M1- phase VO_2 optical phonons and F–P modes.

the pristine and irradiated samples, respectively. The irradiated V-FPRC displays a rougher heterointerface than the pristine sample, indicative of aging-induced interfacial degradation, presumably caused by ion-migration and compositional loss [26]. The EDX elemental profiles along the indicated arrows in Figs. 2(a) and 2(b) are shown in Figs. 2(c) and 2(d), the vacuum ultraviolet irradiation significantly enhances the accumulation of In^+ and Sn^+ at the ITO/VO_2 interface, as well as their subsequent migration into the VO_2 layers. The elemental distributions were compared by EDX mappings in STEM (Figs. 2(e)–2(h)). On close inspection, large accumulations of both indium and tin can be seen for the irradiated V-FPRC along the interface ITO/VO_2 region, and oxygen partitioning (white arrows) between the layers is more significant. These findings are strongly corroborated by quantitative elemental distribution analysis. Next, we performed temperature-dependent conductivity measurement and used the Nernst–Einstein equation (Eq. (1)) to evaluate the ion migration behavior [27]

$$\sigma T = \sigma_0 e^{-E_a/K_B T} \quad (1)$$

where E_a is the activation energy of ion migration, σ is the conductivity, k_B represents the Boltzmann constant, and T is the temperature, respectively. The E_a values are 1.04 and 0.56 eV for the pristine and irradiated V-FPRC, respectively (Fig. S4 and Table S4 in the ESM). The attenuated E_a indicates that the ion migration is significantly enhanced for the irradiated V-FPRC.

HAADF-STEM and SAED measurements were used to analyze the effect of elemental migration on the crystal structure of ITO and VO_2 interface (Figs. 2(i) and 2(j)). In stark contrast to the pristine sample, a more pronounced nanoscale lattice fringe ordering is observed in the irradiated ITO and VO_2 interface. The (222) crystal surface of In_2O_3 is exposed [25], with a surface spacing of 0.29 nm, which corresponds to the SAED result (Figs. 2(i) and 2(j)(I)). Furthermore, compared to the pristine sample, the irradiated ITO surface exhibited reduced grain size and roughness (Figs. S5 and S6 in the ESM), which correlated with decreased sheet resistance and increased carrier concentration and mobility (Fig. S7 in the ESM). The results reveal that irradiation alters the crystallinity of ITO, concomitantly affecting its electrical properties. Then, the VO_2 interplanar spacing evolves from 0.327 nm (M1-phase, (011)) to 0.321 nm (R-phase, (110)) following irradiation. This observation is further corroborated by SAED analysis (Figs. 2(i) and 2(j)(II)), where the pristine VO_2 exhibits distinct diffraction spots corresponding to the (011), ($\bar{2}$12), and ($\bar{3}$21) planes of the M1-phase, while the irradiated VO_2 displays diffraction patterns assignable to the (110), (001), (111), and (021) planes of the R-phase. These structural changes correlate well with the GIXRD results.

2.3 Analysis of ITO/VO_2 heterojunction internal phase characteristics

Figures 3(a) and 3(e) further analyze the regions distal to the interface, with yellow and green dotted lines denoting the ITO and VO_2 layers, respectively. HAADF-STEM reveals well-defined lattice fringes in both pristine and irradiated ITO, showing no significant structural alteration (Figs. 3(b) and 3(f)). The irradiated ITO layer

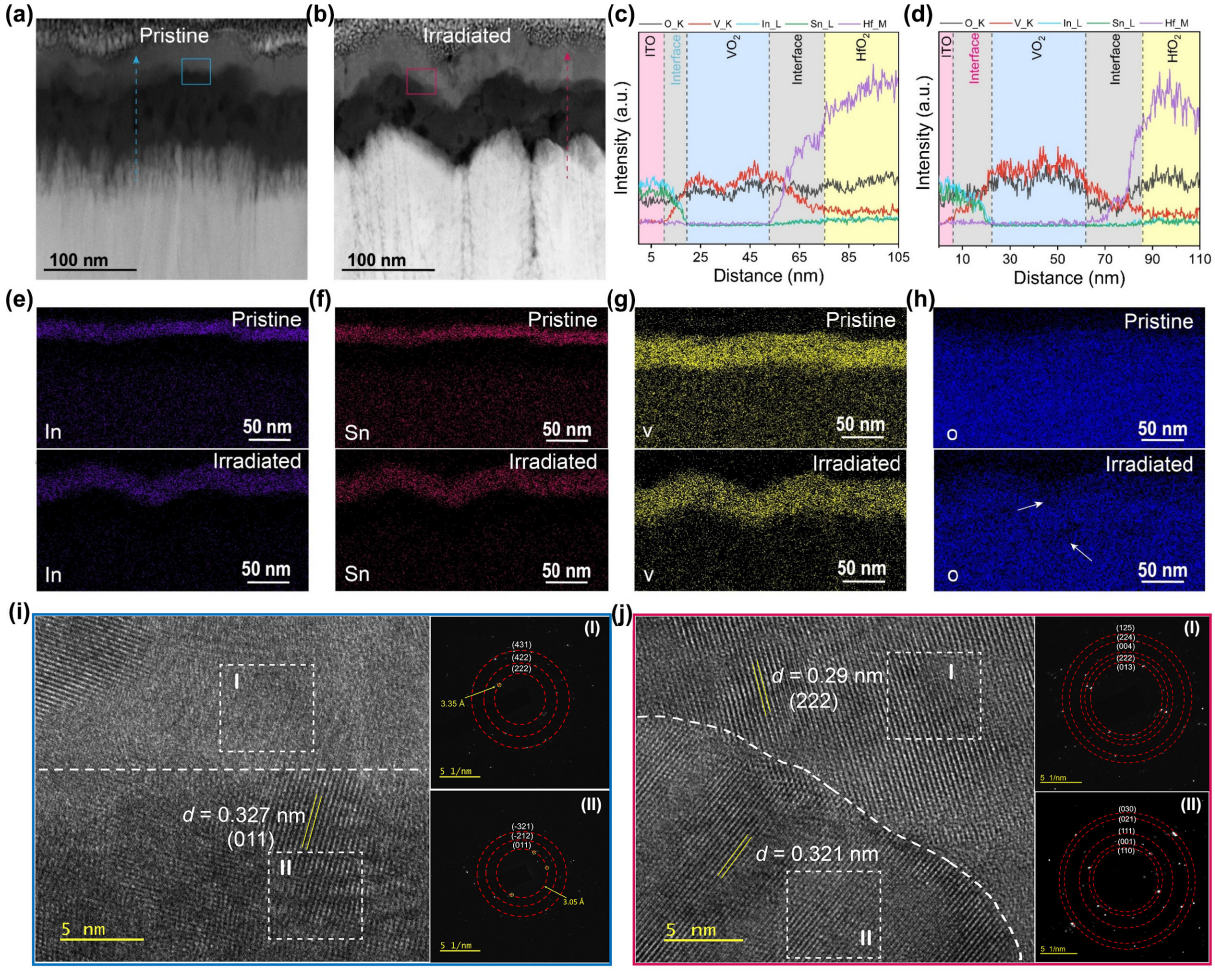

Figure 2 Characterization of ITO/VO_2 interface morphology and crystal structure of the pristine and irradiated V-FPRC. (a) and (b) Cross-sectional STEM images of the pristine and irradiated V-FPRC. (c) and (d) EDX elemental profiles along the indicated arrows in panels (a) and (b), respectively. (e)–(h) EDX elemental maps of indium (e), tin (f), vanadium (g), and oxygen (h) for pristine and irradiated V-FPRC cross-sectional STEM samples. (i) HAADF-STEM and SAED images of the domains of the pristine ITO/VO_2 interface. (j) HAADF-STEM and SAED images of the domains of the irradiated ITO/VO_2 interface.

presents an enhanced (222) plane spacing of 0.306 nm than that of the pristine sample (0.302 nm) (Fig. S8 in the ESM), which corresponds to the lattice expansion of 1.3%. In the VO_2 layer, atomic-resolution HAADF images in Figs. 3(c) and 3(g) reveal the well-ordered arrangement of V atoms, both before and after irradiation. The observed structural modifications V–V spacings evolving from 2.72/3.15 to 2.91/2.95 Å (Figs. 3(d) and 3(h)) and interatomic angle reduction (84° to 79°) quantitatively match the characteristic structural signature of the VO_2 M1-R phase transition, demonstrating irradiation-induced phase transformation [28, 29]. To elucidate the influence of ITO crystal structure modifications on the local strain and lattice distortion in VO_2, we conducted geometric phase analysis (GPA) on the HAADF-STEM images. Color mapping of the strain distribution identifies red regions as tensile-strained and blue regions as compressive-strained. Figure S9 in the ESM shows the in-plane strain (E_{xx}) and out-of-plane strain (E_{yy}) along the direction of [111] of In_2O_3, respectively. The local strain evolution reveals that irradiation induces compressive lattice distortion along the in-plane direction (E_{xx}), tensile distortion along the out-plane direction (E_{yy}), and enhanced strain inhomogeneity (E_{xy}). Correspondingly in the VO_2 layer, the GPA shows that the tensile strain E_{xx} in the direction of [101] increased after irradiation, while the E_{yy} strain fluctuation decreased, and the overall uniformity became better (Fig. S10 in the ESM). Thus, the migration of In, Sn, and oxygen vacancies alters the local bonding environment and induces lattice distortion in VO_2. This structural perturbation modifies the M1-to-R transformation, which arises not from strain or defect doping alone, but from their combined effect.

To explore the variation in vanadium's coordination structure before and after UV-irradiation, the k^2-weighted Fourier transforms of the V K-edge EXAFS and the corresponding fitting curves without phase correction in R-space were employed. As shown in Figs. 3(i) and 3(j) and Fig. S11 in the ESM, the V–O bond length (2.05 Å) becomes longer and the V–V bond length becomes 3.01 Å after irradiation compared to the peaks at 1.84 Å (V–O), 2.43 Å (V–V, dimer), 3.14 Å (V–V, adjacent V atoms in the chain), and 3.45 Å (V–O–V) of the pristine, and the parameters are detailed in Table S3 in the ESM. Similarly, the EXAFS of the wavelet transform (Figs. 3(k) and 3(l)) further reveals the evolution of the intensity of the V–O, V–V dimer, and V–O–V regions in the K-space. After irradiation, the disappearance of the V–V dimer signal (intrachain sub-neighbor V) bond at about 6 $Å^{-1}$ further confirmed the emergence of the vanadium coordination structure of R phase VO_2. Notably, the V K-edge absorption edge remains unchanged (Fig. S12 in the ESM), indicating that the vanadium oxidation state

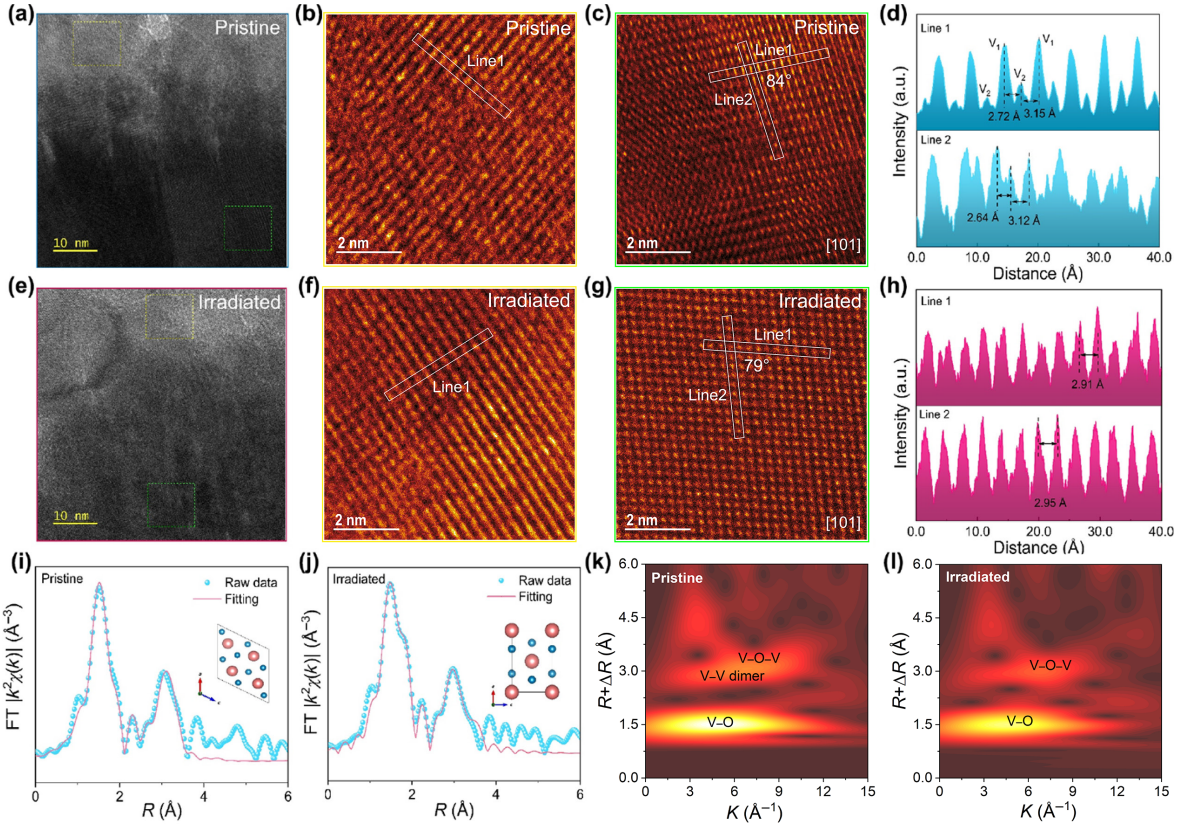

Figure 3 Atomic-level analysis of ITO and VO_2 layers of the pristine and irradiated V-FPRC. (a) and (e) Cross-sectional STEM images of the pristine and irradiated of ITO and VO_2 layers. (b) and (f) HAADF-STEM images of the pristine and irradiated ITO layer. (c) and (g) HAADF -STEM images along [101] direction of the pristine and irradiated VO_2 layer. (d) The line intensity profiles, taken from (c), correspond to lines observed in HAADF-STEM image of VO_2. (h) The line intensity profiles, taken from (g), correspond to lines observed in HAADF-STEM image of VO_2. (i) and (j) Fitting curves of V K-edge FT-EXAFS spectra of the pristine and irradiated VO_2 layer at *R* space. (k) and (l) k^2-weighted WT EXAFS signals of the pristine and irradiated VO_2 layer at V K-edges.

persists as V^{4+} before and after irradiation (Fig. S12 in the ESM). These observations suggest that the bulk VO_2 phase transition is likely induced by lattice strain resulting from interfacial element diffusion [30]. The above evidence demonstrates that the irradiation-induced modification of ITO's crystallographic and elemental migration properties drives a VO_2 phase transition from M1 to R, occurring not only at the ITO/VO_2 interface but also throughout the bulk VO_2 layer.

2.4 Mechanism of UV-induced VO_2 heterojunction phase transition

Deep etching X-ray photoelectron spectroscopy (XPS) characterizations were carried out to investigate the interaction between ITO and VO_2 layers after irradiation. The signal mappings of In, Sn, O, V, and W exhibit depth-dependent variations, as illustrated in Fig. S13 in the ESM, In and Sn signals attenuated beyond 40–50 nm, whereas V and W signals appeared at ~ 30 nm, with all four elements showing pronounced interdiffusion in the irradiated specimen. To probe irradiation-induced effects, we analyzed the binding energy shifts of In, Sn, and O (ITO layer, 20 nm depth) before and after irradiation, along with those of V, W, and O (VO_2 layer, 80 nm depth). The In 3d peak and Sn 3d peak of irradiated sample exhibit a downward shift to lower binding energies by 0.5–0.6 eV (Figs. 4(a) and 4(b)). The O 1s of ITO peaks shift to higher binding energies by 0.7 eV (Fig. 4(c)). Correspondingly, the O 1s of VO_2 peaks shift to higher binding energy by 0.5 eV (Fig. 4(d)), and both the V 2p peak and the W 4f peak exhibit a notable decrease of 0.3–0.5 eV in the low binding energy region (Fig. S14 in the ESM). Additionally, electron paramagnetic resonance (EPR) spectroscopy results revealed a 13% increase in the sharp signal peak at a *g*-value of 2.003 in the irradiated sample (Fig. 4(e)). This peak is characteristic of oxygen vacancies (V_o^+) and serves as a definitive signature of oxygen deficiency. The O K-edge XANES spectra analysis, showing a shift of the absorption edge of binding energy towards the low-energy region, further corroborates this finding (Fig. S15 in the ESM). These results indicate that the chemical orbital environment of the ITO and VO_2 layers is altered by the interlayer migration of In^+, Sn^+, and V_o^+ ions subsequent to irradiation.

Density functional theory (DFT) calculations were performed to gain further insights into the charge density and atom orbitals variations. The reduced crystal formation energy in oxygen-deficient M-phase VO_2 implies that oxygen vacancies lower the energy barrier for interfacial In diffusion (Fig. S16 in the ESM). The pristine VO_2 (M1 phase) exhibits an intrinsic band gap of 0.71 eV [31], introduction of In dopants and oxygen vacancies (irradiated) induce a downward shift in the bands near the Fermi level, reducing the band gap to 0.32 eV and enhancing the VO_2's metallic properties (Fig. S17 in the ESM). Charge density difference analysis reveals an enhanced electron density accumulation on the O atoms, resulting from electron donation by the V atoms in pristine VO_2. Visualization of the charge transfer process exhibits a pink equivalence surface near the In atom of the irradiated VO_2, while the O side displayed cyan equivalence surfaces, indicating the more

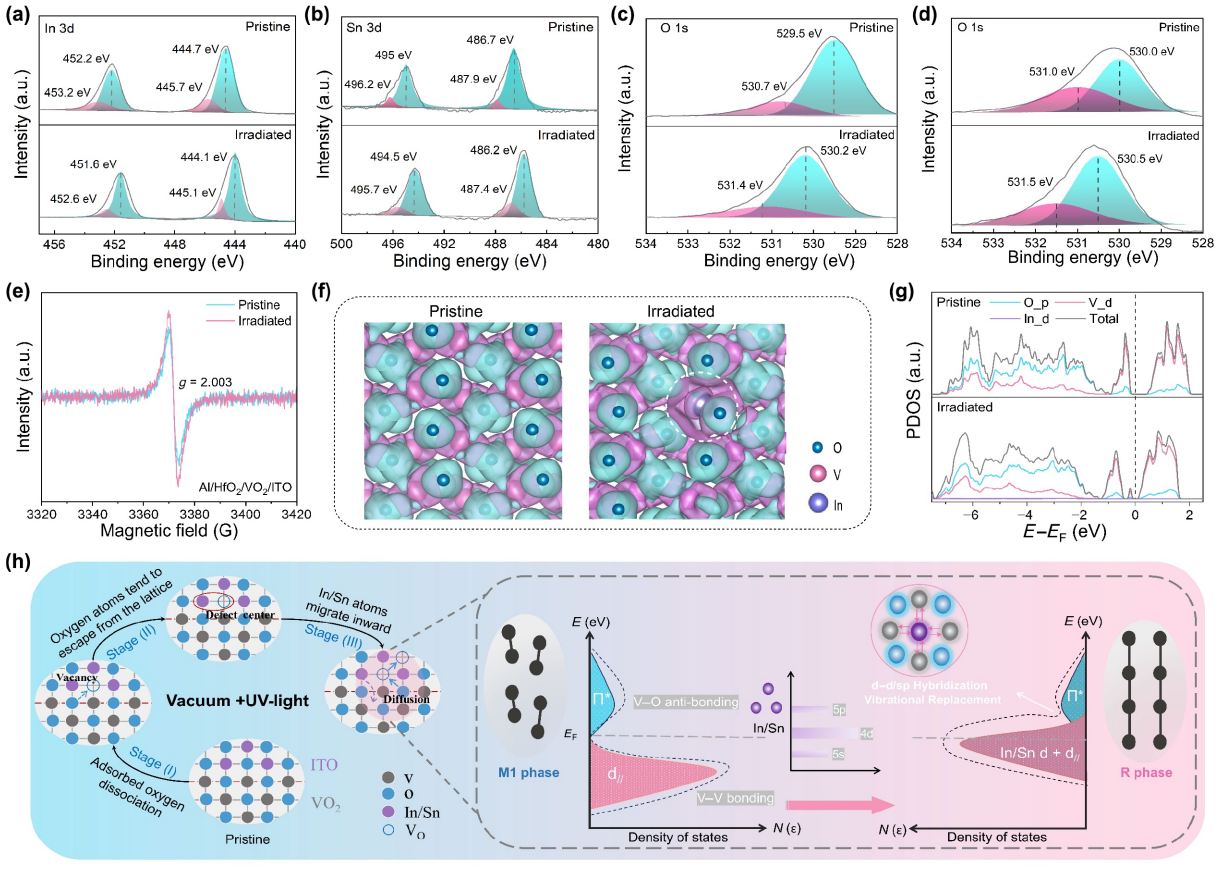

Figure 4 Mechanism of vacuum-UV induced M1-VO_2 phase degradation. XPS spectra of (a) In 3d, (b) Sn 3d, and (c) O 1s of the pristine and irradiated ITO layer. (d) XPS spectra of O 1s of the pristine and irradiated VO_2 layer. (e) EPR spectra of the pristine and irradiated V-FPRC. (f) Surface charge density difference, the cyan and pink regions correspond to an accumulation and depletion of electron density, respectively. (g) Projected density of states (PDOS) of O atom p-orbital, and V, In, Sn atoms d-orbitals of the pristine and irradiated VO_2. (h) Schematic illustration of vacuum-UV induced VO_2 M1-phase to R-phase conversion in the V-FPRC.

electron transfer from In to O (Fig. 4(f)). Figure 4(g) shows the atoms orbital diagram and projected density of states (PDOS) calculations. There are distinct shifts in the density of states in the p-orbitals of O and the d-orbitals of V atoms toward the top of the valence band. Specifically, with respect to the Fermi level, the maximum valence bands of O atomic density of states shifted from 0.49 to 0.13 eV, and V atomic density of states shifted from 0.42 to 0.10 eV, respectively (Fig. S18 in the ESM). After irradiation, the electrons first occupy the lower t_{2g} levels, including the $d_{//}$ and $d_{//}^*/\pi^*$ orbitals, resulting in the Fermi level upshift as well as producing the new defect energy level (Fig. S19 in the ESM).

Based on the evidence of experimental and theoretical calculations, we propose the VO_2 phase transition mechanism in Fig. 4(h). Under vacuum ultraviolet (VUV) irradiation, the oxygen vacancies in the ITO layer initially contain a substantial amount of adsorbed oxygen [32]. Upon irradiation, the adsorbed oxygen atoms acquire sufficient energy to desorb from the surface, leading to ultraviolet-induced outgassing and an increase in surface oxygen vacancy concentration. With prolonged irradiation, some lattice oxygen ions (O^{2-}) in In_2O_3 are released, generating additional oxygen vacancies, while a lower O_2 partial pressure further promotes the formation of doubly ionized oxygen vacancies ($V_{\ddot{O}}$) and defect centers (In-$V_{\ddot{O}}$/Sn-$V_{\ddot{O}}$/V-$V_{\ddot{O}}$). This shift in the reaction equilibrium (Eq. (2)) facilitates interfacial oxygen migration and the formation of oxygen vacancies in the VO_2 layer (Eq. (3)) [33, 34]

$$O_o^X \rightleftharpoons V_o^{\cdot} + 2e' + 1/2O_2 \uparrow \quad (2)$$

$$V_o^{\cdot} \rightleftharpoons V_o + 2\dot{e} \quad (3)$$

Prolonged high-energy UV irradiation further promotes the cleavage of In–O and Sn–O bonds in the ITO layer, which facilitates the interdiffusion and migration of In and Sn. This migration enhances the electron occupancy of the hybridized energy level formed by the $d_{//}$-bond orbital and In/Sn-d orbitals in the V–V dimer. The increased electron density in the $d_{//}$ state strengthens orbital overlap with hybridized π^* antibonding orbitals, ultimately driving the phase transition of VO_2 from the insulating monoclinic (M1) phase to the metallic rutile (R) phase.

3 Conclusion

In summary, our findings reveal, at the atomic scale, the phase-transition mechanism of VO_2 driven by the interlayer diffusion of In, Sn, and V_O under vacuum ultraviolet irradiation in V-FPRC. The interlayer diffusion of elements induces a vibrational displacement of the $d_{//}$ bonding orbital in the V–V dimer. This displacement facilitates orbital overlap with the hybridized π antibonding orbital, ultimately triggering the phase transition of VO_2 from the M1 to the R phase. To further corroborate our experimental findings, DFT calculations were performed, yielding results that consistently validated the experimental observations. These theoretical results provide crucial mechanistic insights into the defects induced VO_2 phase stabilization, while simultaneously establishing a robust foundation for both the rational design of

strongly correlated oxides and future investigations in optoelectronic information science.

Electronic Supplementary Material: Supplementary material (experimental section, experimental and characterization details, density functional theory methodology, and supporting experimental results such as Figs. S1–S20, Table S1–S4) is available in the online version of this article at https://doi.org/10.26599/NR.2026.94908919.

Data availability

All data needed to support the conclusions in the paper are presented in the manuscript and the Electronic Supplementary Material. Additional data related to this paper may be requested from the corresponding author upon request.

Acknowledgements

This work was financially supported by the National Key R&D Program of China (No. 2025YFF0520600), the National Natural Science Foundation of China (No. 52272291), Natural Science Foundation of Jiangsu Province (No. BK20240389), and Jiangsu Funding Program for Excellent Postdoctoral Talent. Besides, the authors would also like to thank Professor Yan Jiang of Beijing Institute of Technology for his valuable suggestions on the manuscript.

Declaration of competing interest

All the contributing authors report no conflicts of interest in this work.

Author contribution statement

Y. L. and T. Z. conceived the idea and designed the experiments. T. Z. was involved in all the experimental parts. Y. Y. C., X. Q. G., Q. Q. Z., J. R. L., and C. L. contributed to the fabrication of the high-performance passive dynamic thermal radiator. Y. F. Y., J. X. G., and S. L. D. helped to optimize the experiments and conduct the characterizations. H. Y. O. Y. carried out the theoretical calculation of the DFT. Y. L., J. P. Z., and T. Z. wrote and revised the manuscript. All authors were involved in the discussion for data analysis and commented on the manuscript.

Use of AI statement

None.

References

[1] Lee, D.; Chung, B.; Shi, Y.; Kim, G. Y.; Campbell, N.; Xue, F.; Song, K.; Choi, S. Y.; Podkaminer, J. P.; Kim, T. H. et al. Isostructural metal-insulator transition in VO_2. *Science* **2018**, *362*, 1037–1040.

[2] Matsuda, Y. H.; Nakamura, D.; Ikeda, A.; Takeyama, S.; Suga, Y.; Nakahara, H.; Muraoka, Y. Magnetic-field-induced insulator-metal transition in W-doped VO_2 at 500 T. *Nat. Commun.* **2020**, *11*, 3591.

[3] Mogunov, I. A.; Lysenko, S.; Fedianin, A. E.; Fernández, F. E.; Rúa, A.; Kent, A. J.; Akimov, A. V.; Kalashnikova, A. M. Large non-thermal contribution to picosecond strain pulse generation using the photo-induced phase transition in VO_2. *Nat. Commun.* **2020**, *11*, 1690.

[4] Dagotto, E. Complexity in strongly correlated electronic systems. *Science* **2005**, *309*, 257–262.

[5] Bhupathi, S.; Wang, S. C.; Ke, Y. J.; Long, Y. Recent progress in vanadium dioxide: The multi-stimuli responsive material and its applications. *Mater. Sci. Eng.: R: Rep.* **2023**, *155*, 100747.

[6] Lanza, M.; Pazos, S.; Aguirre, F.; Sebastian, A.; Le Gallo, M.; Alam, S. M.; Ikegawa, S.; Yang, J. J.; Vianello, E.; Chang, M. F. et al. The growing memristor industry. *Nature* **2025**, *640*, 613–622.

[7] Wang, S. C.; Jiang, T. Y.; Meng, Y.; Yang, R. G.; Tan, G.; Long, Y. Scalable thermochromic smart windows with passive radiative cooling regulation. *Science* **2021**, *374*, 1501–1504.

[8] Yuan, R.; Tiw, P. J.; Cai, L.; Yang, Z. Y.; Liu, C.; Zhang, T.; Ge, C.; Huang. R.; Yang. Y. C. A neuromorphic physiological signal processing system based on VO_2 memristor for next-generation human-machine interface. *Nat. Commun.* **2023**, *14*, 3695.

[9] Tang, K. C.; Dong, K. C.; Li, J. C.; Gordon, M. P.; Reichertz, F. G.; Kim, H.; Rho, Y.; Wang, Q. J.; Lin, C. Y.; Grigoropoulos, C. P. et al. Temperature-adaptive radiative coating for all-season household thermal regulation. *Science* **2021**, *374*, 1504–1509.

[10] Ma, H.; Hou, J. W.; Wang, X. W.; Zhang, J.; Yuan, Z. Q.; Xiao, L.; Wei, Y.; Fan, S. S.; Jiang, K. L.; Liu K. Flexible, all-inorganic actuators based on vanadium dioxide and carbon nanotube bimorphs. *Nano Lett.* **2017**, *17, 1*, 421–428.

[11] Jeong, J.; Aetukuri, N.; Graf, T.; Schladt, T. D.; Samant, M. G.; Parkin, S. S. P. Suppression of metal-insulator transition in VO_2 by electric field-induced oxygen vacancy formation. *Science* **2013**, *339*, 1402–1405.

[12] Morin, F. J. Oxides which show a metal-to-insulator transition at the Neel temperature. *Phys. Rev. Lett.* **1959**, *3*, 34–36.

[13] Asayesh-Ardakani, H.; Nie, A. M.; Marley, P. M.; Zhu, Y. H.; Phillips, P. J.; Singh, S.; Mashayek, F.; Sambandamurthy, G.; Low, K. B.; Klie, R. F. et al. Atomic origins of monoclinic-tetragonal (rutile) phase transition in doped VO_2 nanowires. *Nano Lett.* **2015**, *15*, 7179–7188.

[14] Quackenbush, N. F.; Paik, H.; Wahila, M. J.; Sallis, S.; Holtz, M. E.; Huang, X.; Ganose, A.; Morgan, B. J.; Scanlon, D. O.; Gu, Y. et al. Stability of the M2 phase of vanadium dioxide induced by coherent epitaxial strain. *Phys. Rev. B* **2016**, *94*, 085105.

[15] Ghedira, M.; Vincent, H.; Marezio, M.; Launay, J. C. Structural aspects of the metal-insulator transitions in $V_{0.985}Al_{0.015}O_2$. *J. Solid State Chem.* **1977**, *22*, 423–438.

[16] Yoon, H.; Choi, M.; Lim, T. W.; Kwon, H.; Ihm, K.; Kim, J. K.; Choi, S. Y.; Son, J. Reversible phase modulation and hydrogen storage in multivalent VO_2 epitaxial thin films. *Nat. Mater.* **2016**, *15*, 1113–1119.

[17] Sellers, D. G.; Braham, E. J.; Villarreal, R.; Zhang, B. Y.; Parija, A.; Brown, T. D.; Alivio, T. E. G.; Clarke, H.; De Jesus, L. R.; Zuin, L. et al. Atomic hourglass and thermometer based on diffusion of a mobile dopant in VO_2. *J. Am. Chem. Soc.* **2020**, *142*, 15513–15526.

[18] Geng, C. C.; Chen, Y. Y.; Wei, H.; Zhao, T.; Zhao, Q. Q.; Tian, Z. S.; Dou, S. L.; Liu, Y. F.; Li, Y. Adaptive variable emissivity reflector for seasonal and daily thermal regulation in regions with significant temperature variations. *Adv. Funct. Mater.* **2024**, *34*, 2410819.

[19] Almajhadi, M. A.; Uddin, S. M. A.; Wickramasinghe, H. K. Observation of nanoscale opto-mechanical molecular damping as the origin of spectroscopic contrast in photo induced force microscopy. *Nat. Commun.* **2020**, *11*, 5691.

[20] Sternbach, A. J.; Ruta, F. L.; Shi, Y.; Slusar, T.; Schalch, J.; Duan, G. W.; McLeod, A. S.; Zhang, X.; Liu, M. K.; Millis, A. J. et al. Nanotextured dynamics of a light-induced phase transition in VO_2. *Nano Lett.* **2021**, *21*, 9052–9060.

[21] Abedini Dereshgi, S.; Larciprete, M. C.; Centini, M.; Murthy, A. A.; Tang, K.; Wu, J. Q.; Dravid, V. P.; Aydin, K. Tuning of optical phonons in α-MoO_3-VO_2 multilayers. *ACS Appl. Mater. Interfaces* **2021**, *13*, 48981–48987.

[22] Zhao, T.; Chen, Y. Y.; Gu, J. X.; Wei, H.; Geng, C. C.; Li, X.; Jin, C.

F.; Liang, S. H.; Dou, S. L.; Wang, J. Z. et al. Multifunctional radiation conditioning emitter for laser and infrared with adaptive radiative cooling. *ACS Appl. Mater. Interfaces* **2024**, *16*, 52153–52161.

[23] Wei, H.; Gu, J. X.; Zhao, T.; Yan, Z. Y.; Xu, H. X.; Dou, S. L.; Qiu, C. W.; Li. Y. Tunable VO_2 cavity enables multispectral manipulation from visible to microwave frequencies. *Light: Sci. Appl.* **2024**, *13*, 54.

[24] Gu, J. X.; Wei, H.; Ren, F. F.; Fan, Q. P.; Xu, G. P.; Chen, X.; Song, S. S.; Dou, S. L.; Zhao, J. P.; Li, Y. Fabrication and performances of double-sided HfO_2 anti-reflection films with ultra-high infrared transmittance. *J. Alloys Compd.* **2021**, *858*, 158337.

[25] Yang, S. M.; Sun, B. S.; Liu, Y.; Zhu, J. P.; Song, J. X.; Hao, Z. H.; Zeng, X. Y.; Zhao, X.; Shu, Y. C.; Chen, J. et al. Effect of ITO target crystallinity on the properties of sputtering deposited ITO films. *Ceram. Int.* **2020**, *46*, 6342–6350.

[26] Tan, S.; Huang, T. Y.; Yavuz, I.; Wang, R.; Yoon, T. W.; Xu, M. J.; Xing, Q. Y.; Park, K.; Lee, D. K.; Chen, C. H. et al. Stability-limiting heterointerfaces of perovskite photovoltaics. *Nature* **2022**, *605*, 268–273.

[27] Xing, J.; Wang, Q.; Dong, Q. F.; Yuan, Y. B.; Fang, Y. J.; Huang, J. S. Ultrafast ion migration in hybrid perovskite polycrystalline thin films under light and suppression in single crystals. *Phys. Chem. Chem. Phys.* **2016**, *18*, 30484–30490.

[28] Cui, Y. Y.; Ke, Y. J.; Liu, C.; Chen, Z.; Wang, N.; Zhang, L. M.; Zhou, Y.; Wang, S. C.; Gao, Y. F.; Long. Y. Thermochromic VO_2 for energy-efficient smart windows. *Joule* **2018**, *2*, 1707–1746.

[29] Heckingbottom, R.; Linnett, J. W. Structure of vanadium dioxide. *Nature* **1962**, *194*, 678.

[30] Aetukuri, N. B.; Gray, A. X.; Drouard, M.; Cossale, M.; Gao, L.; Reid, A. H.; Kukreja, R.; Ohldag, H.; Jenkins, C. A.; Arenholz, E. et al. Control of the metal-insulator transition in vanadium dioxide by modifying orbital occupancy. *Nat. Phys.* **2013**, *9*, 661–666.

[31] Fan, L. L.; Chen, S.; Luo, Z. L.; Liu, Q. H.; Wu, Y. F.; Song, L.; Ji, D. X.; Wang, P.; Chu, W. S.; Gao, C. et al. Strain dynamics of ultrathin VO_2 film grown on TiO_2(001) and the associated phase transition modulation. *Nano Lett.* **2014**, *14*, 4036–4043.

[32] Xu, W. D.; Xia, R. D.; Ye, T. L.; Zhao, L.; Kan, Z. P.; Mei, Y.; Yan, C. F.; Zhang, X. W.; Lai, W. Y.; Keivanidis, P. E. et al. Understanding the light soaking effects in inverted organic solar cells functionalized with conjugated macroelectrolyte electron-collecting interlayers. *Adv. Sci.* **2016**, *3*, 1500245.

[33] Zhang, H. T.; Guo, L.; Stone, G.; Zhang, L.; Zheng, Y. X.; Freeman, E.; Keefer, D. W.; Chaudhuri, S.; Paik, H.; Moyer, J. A. et al. Imprinting of local metallic states into VO_2 with ultraviolet light. *Adv. Funct. Mater.* **2016**, *26*, 6612–6618.

[34] Ko, C.; Ramanathan, S. Effect of ultraviolet irradiation on electrical resistance and phase transition characteristics of thin film vanadium oxide. *J. Appl. Phys.* **2008**, *103*, 106104.